A quantum memory at telecom wavelengths

Wallucks, Andreas; Marinković, Igor; Hensen, Bas; Stockill, Robert; Gröblacher, Simon

DOI
10.1038/s41567-020-0891-z

Publication date
2020

Document Version
Final published version

Published in
Nature Physics

nature physics

ARTICLES

https://doi.org/10.1038/s41567-020-0891-z

A quantum memory at telecom wavelengths

Andreas Wallucks, Igor Marinković, Bas Hensen, Robert Stockill and Simon Gröblacher ✉

Nanofabricated mechanical resonators are gaining significant momentum among potential quantum technologies due to their unique design freedom and independence from naturally occurring resonances. As their functionality is widely detached from material choice, they constitute ideal tools for transducers—intermediaries between different quantum systems—and as memory elements in conjunction with quantum communication and computing devices. Their capability to host ultra-long-lived phonon modes is particularity attractive for non-classical information storage, both for future quantum technologies and for fundamental tests of physics. Here, we demonstrate a Duan–Lukin–Cirac–Zoller-type mechanical quantum memory with an energy decay time of $T_1 \approx 2$ ms, which is controlled through an optical interface engineered to natively operate at telecom wavelengths. We further investigate the coherence of the memory, equivalent to the dephasing T_2^* for qubits, which has a power-dependent value between 15 and 112 μs. This demonstration is enabled by an optical scheme to create a superposition state of $|0\rangle + |1\rangle$ mechanical excitations, with an arbitrary ratio between the vacuum and single-phonon components.

Quantum memories are a core quantum technology and are at the very heart of building quantum repeaters and thus enabling large quantum networks[1,2]. Significant progress on realizing such memories has been made with ions[3,4], atomic ensembles[5–7], single atoms[8], nitrogen-vacancy centres[9] and erbium-doped fibres[10]. The important characteristics of a memory, besides sufficiently long storage times, are the ability to store a true quantum state, such as a single photon, high readout efficiency, on-demand retrieval and operation at low-loss telecommunication wavelengths around 1,550 nm. So far, none of the realizations have simultaneously been able to demonstrate all of these requirements. In particular, native operation of memories in the telecom band has been limited to classical states[11,12] or storage times in the tens of nanoseconds[13].

Recently, chip-based nanoscale mechanical resonators have emerged as promising components for future quantum technologies. Their functionality is principally based on geometry, allowing for great flexibility in materials and designs and creating unique opportunities for combining them with many other techniques such as integrated photonics and superconducting circuitry[14,15]. Over the past few years, experiments have demonstrated an ever increasing control over quantum states of mechanical resonators both via optical as well as electrical interfaces. Experimental breakthroughs with radiofrequency drives include electromechanically induced entanglement[16,17], phonon-number detection[18,19] and single-[20] as well as multi-phonon Fock state generation[21]. Optical control over the modes, on the other hand, has enabled the detection of non-classical optomechanical correlations[22–24], single-phonon Fock state creation[25,26], mechanical entanglement[27,28], as well as an optomechanical Bell test[29]. Excitingly, many of these chip-based devices have also been shown to host ultra-long-lived mechanical modes with down to wavelength-scale footprints and low crosstalk[30–32]. Combined, these results demonstrate the key ingredients for the realization of a quantum optomechanical memory, potentially paving the way to on-chip, integrated quantum transducers and repeaters, operating at telecom wavelengths[33,34].

In this Article, we demonstrate non-classical correlations from an engineered high-Q mechanical resonance and an optical interface in the conventional telecom band over the full decay time of the mechanical mode. To achieve this, the mechanical quantum memory is prepared in a single-phonon state, directly usable for a Duan–Lukin–Cirac–Zoller-type (DLCZ) quantum repeater scheme[35]. We show that we can store this state for ~2 ms without degradation due to induced thermal occupation of the mode, a limitation of several previous experiments[25,28,29]. We study the phase fluctuations of the mechanical mode in a classical continuous interference measurement and then by a pulsed dephasing experiment in the quantum regime. For the latter, we develop and experimentally demonstrate a scheme to herald superpositions of the first mechanical Fock state and the vacuum. This stored state is then optically retrieved and interfered with a weak coherent probe to measure the coherence of the mechanical mode.

Our device design, shown in Fig. 1, is based on previous experiments with silicon optomechanical crystals[22,25,30], which were optimized for low mechanical quality factors Q_m to speed up re-thermalization with the cryogenic environment. In contrast, in our present work the mechanical mode serves as a phononic memory for optical states and we are hence looking for large quality factors. In particular, the mechanical decay time sets a bound on the distance over which light can travel while the stored state has not yet decayed. For a 1 ms decay time, for example, we can reach distances of ~200 km. The mechanical mode of the silicon nanobeam is confined within a phononic-crystal mirror region that does not exhibit a complete bandgap. Fabrication imperfections typically couple the phonon mode of interest to leaky modes with different symmetries, such that the quality factor is limited by radiation loss. For this experiment, we surround the device with a two-dimensional (2D) phononic shield, which features a complete bandgap[30] and can increase the decay time up to several seconds[32]. Figure 1a shows the fabricated device with the additional phononic shielding region on the sides and an optical waveguide on top used to probe the device. A simulation of the bandstructure of the shield region in Fig. 1b shows a wide bandgap emerging between 4 GHz and 6 GHz.

The actual device used in this experiment has a mechanical resonance at $\Omega_m/2\pi = 5.12$ GHz with a measured decay time of the mode of $2\pi/\Gamma_m = 1.8$ ms (see Supplementary Information), corresponding to a quality factor of $Q_m \approx 1 \times 10^7$ at mK temperatures. Although we have fabricated structures with significantly better values of Q_m ($\gtrsim 1 \times 10^9$), this particular choice is a compromise between long memory time and a low re-initialization rate, which would in

Kavli Institute of Nanoscience, Department of Quantum Nanoscience, Delft University of Technology, Delft, The Netherlands. ✉e-mail: s.groeblacher@tudelft.nl

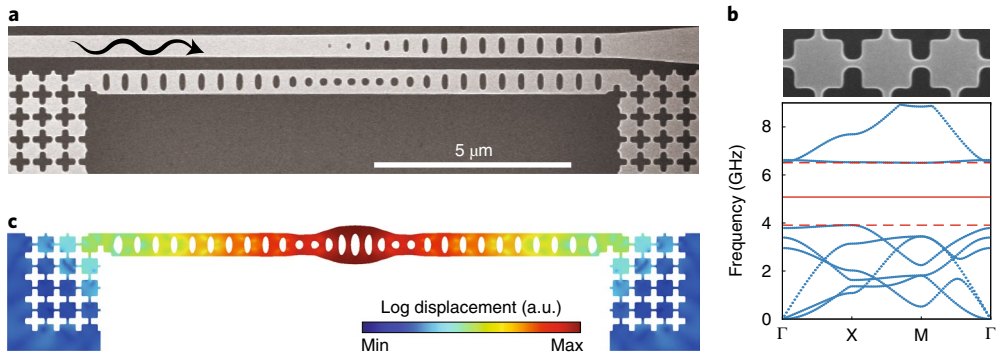

Fig. 1 | Design of the optomechanical quantum memory. a, Scanning electron microscope image of the optomechanical device. Light enters from the left through the coupling waveguide in the top part of the image. In the device below, an optical and a mechanical resonance are coupled through radiation pressure effects. The structure is fabricated from a 250-nm-thick silicon layer and is undercut to produce free-standing devices. **b**, Magnified view of the phononic shield region (top) and corresponding bandstructure simulation (bottom). Unlike the nanobeam itself, the shielding region exhibits a full bandgap of the phononic crystal around the resonance frequency Ω_m (solid red line). **c**, Finite-element simulation of the isolation through the phononic shield. Also shown is the mechanical mode of interest at 5.12 GHz in the centre of the nanobeam.

turn necessitate a prohibitively long measurement time. The optical resonance of the device is at $\omega_c/2\pi = 191.4$ THz, corresponding to a wavelength in the telecom band at 1,566.4 nm, with an intrinsic optical linewidth of $\kappa_i/2\pi = 460$ MHz. As shown in Fig. 1a, we couple to this resonance via an adjacent optical waveguide with a coupling rate of $\kappa_e/2\pi = 1{,}840$ MHz. The optical and mechanical modes interact with a single photon coupling rate $g_0/2\pi = 780$ kHz.

A sketch of the fibre-based optical set-up is presented in Fig. 2a, where the device is placed in a dilution refrigerator with a base temperature of 15 mK. We generate 40-ns-long optical pulses with blue sideband detuning from the optical resonance $\omega_b = \omega_c + \Omega_m$, as well as red sideband detuning $\omega_r = \omega_c - \Omega_m$. Using linearized optomechanical interactions[36,37], blue driving enables optomechancial pair generation $\hat{H}_b = -\hbar g_0 \sqrt{n_b}\hat{a}^\dagger \hat{b}^\dagger + \text{h.c.}$, where n_b is the intracavity photon number, ħ the reduced Planck constant and $\hat{a}^\dagger$ ($\hat{b}^\dagger$) the optical (mechanical) creation operator. Red detuning on the other hand enables a state transfer between the optics and the mechanics due to the beamsplitter-type interaction $\hat{H}_r = -\hbar g_0 \sqrt{n_r}\hat{a}^\dagger \hat{b} + \text{h.c.}$, where n_r is the intracavity photon number for the red pulses. After interacting with the device in the cryostat, the light passes an optical filter with 40 MHz bandwith that is locked to the optical resonance ω_c and the Stokes/anti-Stokes fields are detected on a superconducting nanowire single-photon detector.

As a first step, we performed a thermometry measurement to validate that the 5 GHz mode of the device is thermalized to its motional ground state at the base temperature of the cryostat. This is done by sending trains of either blue or red sideband detuned pulses to the device, such that an asymmetry in the scattering rates between the blue and the red drives allows us to infer the mechanical mode occupation[22,38]. The measured mode temperature is elevated from the bath temperature due to heating caused by power-dependent optical absorption of the drives. We can thus use this measurement to determine our maximally attainable driving power for a given mechanical mode occupation. We limit the instantaneous heating caused by a single pulse to ~0.1 phonons, which we attain with a pulse energy of 280 fJ. This corresponds to a state-transfer probability of $P_r = 14\%$ between phonons and photons in the anti-Stokes field by the red-detuned drive using the interaction of $\hat{H}_r$. The total detection efficiency of the scattered photons is 13%, as discussed in the Supplementary Information, including contributions from the collection efficiency into the device waveguide, fibre coupling, losses in the filter set-up and imperfect detectors.

To test the performance of the device as a quantum memory, we used a two-pulse protocol with a blue-detuned excitation followed by the red-detuned readout pulse. The first pulse enables the optomechanical pair generation according to $\hat{H}_b$, producing entanglement between the optical Stokes field and the mechanical mode of the form

$$|\psi\rangle_{om} \propto |00\rangle_{om} + \sqrt{P_b}|11\rangle_{om} + \mathcal{O}(P_b) \quad (1)$$

where o (m) indicates the optical (mechanical) mode and P_b is the excitation probability. Due to the correlations in this state, detecting a Stokes photon after the blue pulse heralds the mechanical mode in a state close to a single-phonon Fock state[25]

$$|\Psi\rangle_m \propto |1\rangle_m + \mathcal{O}(\sqrt{P_b}) \quad (2)$$

Crucially, the excitation probability P_b has to be kept small to avoid higher-order excitation terms. Additionally, residual absorption heating causes an increased thermal background of the mechanical mode at delays far longer than the pulse length. We choose an energy of the blue-detuned pulse of 3 fJ, which corresponds to a scattering probability of $P_b = 0.2\%$. This optical power is chosen to limit the peak of the absorption heating to below 0.2 phonons occupancy, at most. In Fig. 2c, we show the calibrated mode occupation, highlighting an increase in phonon occupancy for delays of up to 1 ms before the device rethermalizes.

With this limited thermal background, we are able to study the quantum nature of the optomechanically prepared state of equation (2). We do this using the cross-correlation $g^{(2)}_{om} = P(B \wedge R)/[P(B)P(R)]$, where $P(B)$ ($P(R)$) is the probability to detect a Stokes (anti-Stokes) photon and $P(B \wedge R)$ is the joint probability to detect a Stokes and an anti-Stokes photon in one trial. We probe the ability of the mechanical mode to store non-classical correlations by evaluating $g^{(2)}_{om}(\Delta\tau)$ for pulse delays $\Delta\tau$ over the energy decay time of the mechanical resonance. Generally, we expect the cross-correlation to evolve like $g^{(2)}_{om}(\Delta\tau) = 1 + \exp(-\Gamma_m \Delta\tau/2)/n_{therm}(\Delta\tau)$ (ref. [28]), where Γ_m is the inverse of the decay time and $n_{therm}(\Delta\tau)$ the number of thermal phonons in the mode. We note that this cross-correlation has a classical bound given by a Cauchy–Schwarz inequality of $g^{(2)}_{om} \leq 2$ (refs. [22,26]). An even stronger bound can be motivated by considering the threshold required to violate a Bell inequality for the entanglement present in the system (equation (1)), which is given by $g^{(2)}_{om} \geq 5.7$ (refs. [29,39]). Figure 2d shows the measured cross-correlations together with the theoretically expected correlation (solid line) that we calculate using the measured thermal

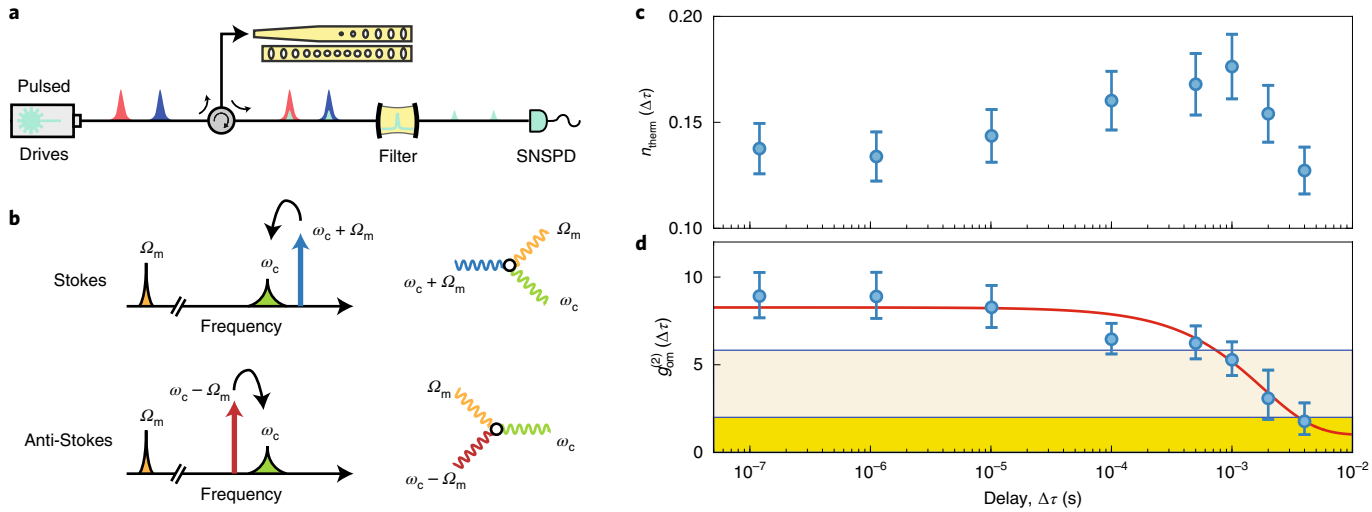

Fig. 2 | Characterization of the memory lifetime and optical heating. a, Laser pulses are sent to the optomechanical device through an optical circulator. These pump pulses are subsequently filtered, allowing us to measure their Stokes and anti-Stokes fields in a superconducting nanowire single-photon detector (SNSPD). **b**, Scattering scheme for the Stokes (top) and anti-Stokes (bottom) processes. Here, Ω_m denotes the mechanical frequency and ω_c the cavity frequency. **c**, Calibrated thermal mode occupancy, showing a delayed rise in the absorption heating from a blue-detuned pulse with energy 3 fJ and probed by a red-detuned pulse with energy of 280 fJ. The occupation contains a background of ~0.1 phonons added by the red drive during the readout. **d**, We verify the suitability of our optomechanical device as a quantum memory by measuring the decay time of the cross-correlations between the Stokes and anti-Stokes fields $g^{(2)}_{om}$ (see main text for details). We find clear non-classical photon–phonon correlations up to $T_1 = 1.8 \pm 0.2$ ms. The classical bound, above which the single phonon that is stored in the mechanical mode still retains its quantum character, is highlighted by the yellow-shaded region, while the beige region depicts the threshold for violating a Bell-type inequality. The red curve is the theoretically predicted decay, for which we use the thermal occupation measured in **c**. All error bars are 1 s.d.

occupation. We find that the classical threshold (yellow-shaded region) is violated by the Stokes and anti-Stokes fields for $T_1 = 1.8 \pm 0.2$ ms. Furthermore, the Bell threshold (beige-shaded region) is violated for ~500 µs, supporting the prospect of using mechanical quantum memories in a device-independent setting[40].

The above measurements clearly demonstrate that, although absorption heating is still present in the device, we can limit its effects to be able to store and retrieve quantum states in the mechanical mode for its whole decay time. As the scheme uses a phase-symmetrical state of the form of equation (2), we are, however, not sensitive to frequency fluctuations of the mechanical mode. We therefore proceed to test the ability of our device to preserve non-trivial quantum mechanical states.

We begin by assessing the frequency stability of the mechanical mode in the classical regime. As discussed in the Supplementary Information, direct measurements of the mechanical sidebands on a fast photodector using a relatively strong continuous sideband drive show a broadened mechanical linewidth of several kHz. A frequency jitter of the mechanical mode is visible using fast scanning[32]. To determine the extent to which optical driving influences these dynamics, we require a measurement scheme that employs a minimum possible intracavity power. We devise an interferometric scheme based on coincidence detection in continuous-wave (c.w.) driving, as shown in Fig. 3a. We probe the device with a single optical tone on either the red or the blue sideband, such that the reflected light contains an optomechanically generated sideband. This sideband is interfered with a probe field at roughly ω_c, which we create in-line from the reflected optical drives using an electro-optic amplitude modulator (EOM). To be able to detect photons using the SNSPDs, we remove the background with a 40 MHz bandwidth filter. The main idea of the measurement is that mixing of the mechanically and electro-optically generated sidebands causes intensity modulations at their beat frequency, which can be observed in the coincidence rate $C^{(2)}(\Delta\tau)$ of the detected photons. The interference can be demonstrated explicitly by detuning the EOM drive by $\delta\Omega/2\pi = 100$ kHz from the mechanical frequency Ω_m, such that $C^{(2)}(\Delta\tau)$ shows oscillations with a period of $2\pi/\delta\Omega = 10$ µs (Fig. 3b). With the mechanical mode in a thermal state, we can measure the decay of this interference to extract a classical coherence time τ_{class} by fitting an exponentially decaying sine function to the data (solid line). Additional details on the data evaluation as well as measurements of the thermal bunching of the optomechnical photons are discussed in the Supplementary Information.

Figure 3c shows the dependence of the coherence time τ_{class} for a sweep of the intracavity photon number n_c. Measurements for blue detuning (blue points) and red detuning (red points) split with increasing photon numbers due to optomechanical damping (for a discussion see Supplementary Information). Inconsistent with residual optomechanical effects, however, is the decrease of the decay constant τ_{class} for the lowest photon numbers. A linear extrapolation to $n_c = 0$ results in $\tau_{class,min} = 16 \pm 3$ µs. The behaviour for $n_c > 1$ can be explained by a saturation of the decay constant for high photon numbers. We fit the power dependence to a phenomenological model (solid line) that we discuss in the Supplementary Information. From the model we obtain a saturation value of $\tau_{class,max} = 112 \pm 27$ µs.

The power dependence observed for the classical coherence decay τ_{class} invites an investigation of the coherence time in the quantum regime, where, additionally, the mode evolves in the dark. In contrast to the above pulsing scheme (Fig. 2), we are now required to measure the phase stability of non-symmetric mechanical quantum states. A natural candidate comprises superpositions between the vacuum and single-phonon mechanical states of the form

$$|\Psi\rangle_m = \sqrt{1-n}|0\rangle_m + \sqrt{n}e^{i\phi}|1\rangle_m \quad (3)$$

Here, ϕ is an experimentally chosen phase during the state preparation and $\sqrt{n}$ is the amplitude of the single-phonon component, with

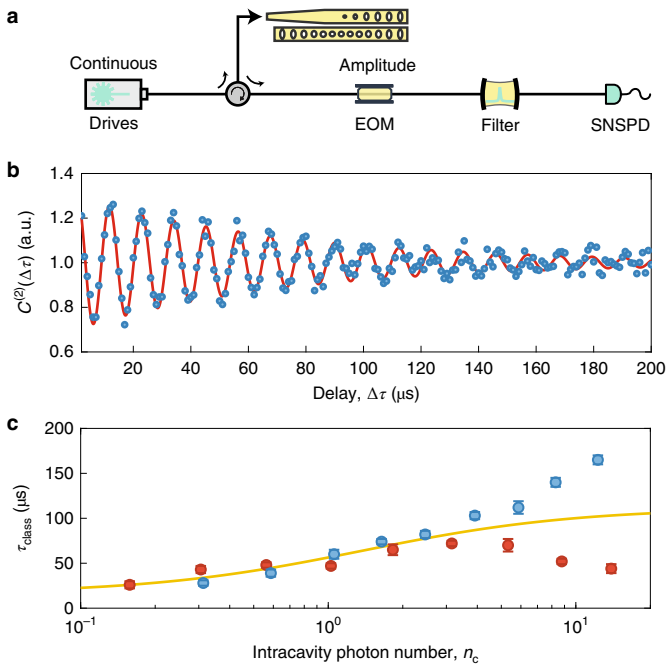

Fig. 3 | Continuous-wave measurement of the mechanical coherence. **a**, Schematic of the set-up for measuring the mechanical phase coherence with a c.w. laser by mixing Stokes and anti-Stokes fields from the device with an electro-optically generated tone. Under continuous driving, the mechanical mode is highly excited and the measurement is therefore fully in the classical regime. The amplitude EOM is driven at a detuning of $\delta\Omega/2\pi = 100$ kHz from the mechanical frequency Ω_m. **b**, Interference between the optomechanically and the electro-optically generated sidebands causes an oscillatory signature in the twofold coincidence rate $C^{(2)}(\Delta\tau)$. Shown is an example measured trace for ~3 intracavity photons (dots) and a fit to the data (solid curve) for a sinusoidal oscillation with exponentially decaying amplitude. The raw data and details on the post-processing are provided in the Supplementary Information. **c**, The extracted decay times τ_{class} as a function of intracavity photon numbers n_c for blue detuning (blue points) as well as for red detuning (red points). An increase in the measured coherence time as a function of intracavity photon number can clearly be seen (the fit to the data is shown as a solid curve). For $n_c \gtrsim 2$, optomechanical effects become visible. All error bars are 1 s.d.

$n = 1/2$ indicating a 50:50 superposition state. Once the mechanical mode is prepared in such a state, it can be read out after a variable delay $\Delta\tau$ and the anti-Stokes field can be interfered with a weak coherent state (WCS), for example. The visibility of this interference can then be used to assess the coherence time T_2^* over which the mechanical mode is able to preserve the phase of the superposition state. The scheme we describe in the following is conceptually similar to earlier experiments in quantum optics[41,42] and enables the optical preparation of a massive mechanical superposition state for the first time.

We adapted the set-up for the correlation decay measurements, adding an optical interferometer in the detection path (Fig. 4a). The light is split by a 99:1 fibre coupler and enters a Mach–Zehnder interferometer with a high-transmission upper arm and a low-transmission lower arm. In the low-transmission arm of the interferometer, an EOM modulates the reflected blue drive to produce a sideband at ω_c (more than 20 dB bigger than the optomechanical one in this arm). This weak coherent state is then interfered with the optomechanically generated sideband in the upper arm of the interferometer on a balanced fibre coupler. Both of its outputs pass 40 MHz bandwidth filter set-ups to remove unwanted frequencies so as to only detect fields at ω_c. A click on one of the SNSPDs heralds the superposition state of equation (3) of the mechanical mode, as the Stokes sideband is made indistinguishable from the electro-optically generated weak coherent state. In a quantum picture, the second beamsplitter removes all 'which-path' information of the detected photons.

The detection is performed after a variable delay by interfering the anti-Stokes fields from the device with another weak coherent state generated from the red drive with the EOM in the lower arm. The quantum interference of the two can be detected through oscillations of the correlation coefficient $E = \left(g^{(2)}_{om,sym} - g^{(2)}_{om,asy}\right) / \left(g^{(2)}_{om,sym} + g^{(2)}_{om,asy}\right)$ of the cross-correlations $g^{(2)}_{om,sym}$ for detection events in the same detectors and $g^{(2)}_{om,asy}$ for different detectors. Although we have to ensure phase stability of the Stokes and anti-Stokes fields and the respective WCSs, we only have to stabilize the Mach–Zehnder interferometer, because path-length fluctuations from the device to the first fibre coupler are cancelled due to the fields propagating in common mode. Similar to the classical coherence measurement, the requirement to actively change the interferometer phase to detect the interference can be alleviated by slightly detuning the EOM drive frequency from Ω_m. We chose a relative detuning of $\delta\omega/2\pi = 1$ MHz, which is again much smaller than the bandwidth of the optical pulses of ~25 MHz but enables a full 2π phase sweep of E for delays of 1 μs.

The amplitude n of the superposition state can be chosen experimentally by adjusting the ratio of optomechanically to electro-optically generated photons in the sidebands. Without a thermal background on the mechanical mode, it is possible to prepare states of the form of equation (3) with a given single-phonon amplitude n by matching the count rate due to the WCS, C_{WCS}, to the Stokes count rate, C_b, according to $C_{WCS}/C_b = (1-n)/n$. In our measurements, the amplitude of the WCS is set to optimize for maximum visibility and detection rates at the same time, which allows us to perform the mechanical coherence measurements as quickly as possible. In the Supplementary Information, we provide further numerical studies on how the choice of amplitude affects the expected interference visibility in the presence of a thermal background on the mechanical mode. Experimentally, we choose the same pulse energies for the red and blue drives as in the correlation measurement (Fig. 2). We adjust the EOM drive power such that $C_{WCS}/C_b \approx 7$, which, for a thermal background of $n_{therm} = 0.1$, results in a single phonon Fock amplitude, $n = 0.56$. The second WCS is matched in power to the anti-Stokes field. Figure 4c shows our experimentally measured correlation coefficient E. A clear oscillation in the signal with the expected period of $2\pi/\delta\omega = 1$ μs can be seen for small delays $\Delta\tau$ around 1 μs, demonstrating the successful interference of the superposition state in the anti-Stokes field with the WCS. We obtain a visibility of $V = 58 \pm 5\%$ by fitting the signal between 1 μs and 2 μs with a sinusoidal function. This visibility exceeds the classical threshold of $V_{class} = 50\%$ for the second-order interference visibility of two coherent states and is in good agreement with the theoretically expected value of 63% (see Supplementary Information).

We plot the decay of the interference visibility for extended delays in Fig. 4d. The quantum coherence time of the state that we obtain from fitting an exponential decay is $T_2^* = 15 \pm 2$ μs. This decay happens much faster than the measured T_1 for the symmetrical state. The obtained value is in very good agreement with the classical coherence time $\tau_{class,min} = 16 \pm 3$ μs, considering the intracavity photon number averaged over the duty cycle in the pulsed experiment is $n_{pulse,avg} \approx 1 \times 10^{-8}$ (Fig. 3c). As shown before, the power dependence of the coherence time is not consistent with optomechanical effects. The observed saturation at $\tau_{class,max}$ indicates

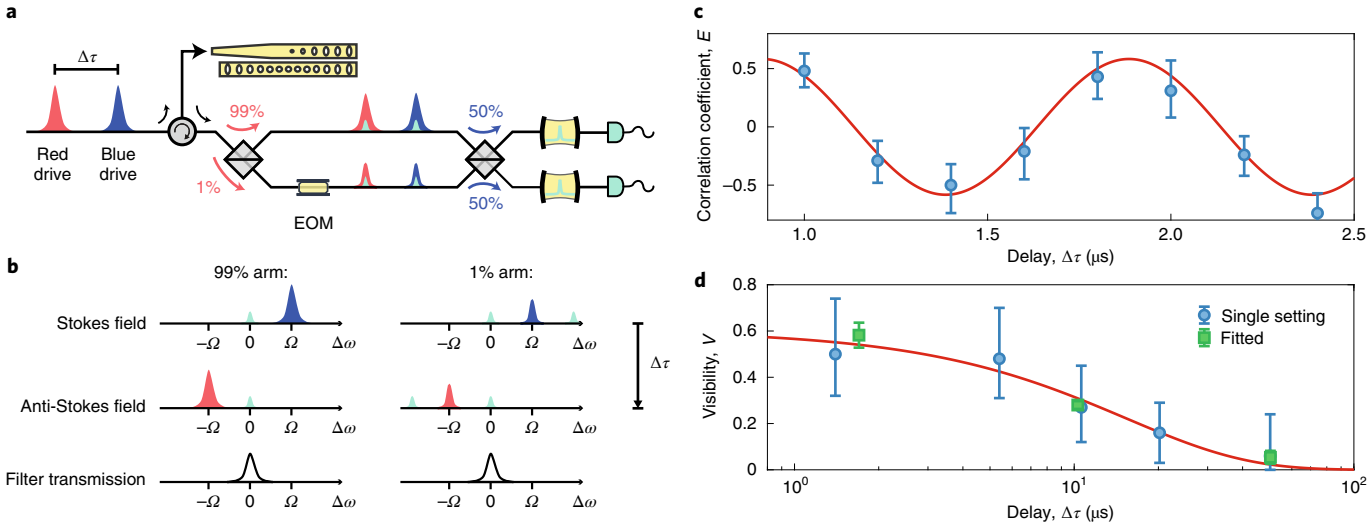

Fig. 4 | Quantum phase coherence of the mechanical memory. a, Sketch of the experimental set-up for the coherence measurement of the quantum memory. After being reflected from the device, the optical pulses are sent to an imbalanced Mach–Zehnder interferometer. In the lower, highly attenuated arm, an EOM creates a WCS at the cavity frequency (ω_c) by sideband modulation of the reflected drives. The WCS is then interfered with the optomechanical Stokes field from the upper, weakly attenuated interferometer arm. All 'which-path' information is erased, such that a detection event on either of the detectors (SNSPDs) heralds a superposition state of the form shown in equation (3). The state is retrieved from the device using a red-detuned drive and the interference of the anti-Stokes field with a second WCS generated with the same EOM is measured. **b**, Schematic depicting the frequency components in the interferometer by their detuning $\Delta\omega$ from the optical resonance. The high-transmission arm contains the optical drives as well as the Stokes or anti-Stokes fields. In the low-transmission arm, the sidebands generated by the EOM dominate over the optomechanically scattered photons. After filtering, only the light on resonance with the optical cavity is detected in the SNSPDs. **c**, Interference of the anti-Stokes field with a WCS after a delay from the blue pulse of $\Delta\tau \approx 1\,\mu s$. Phase evolution over the delay is enabled by detuning the EOM drive by $\delta\omega/2\pi = 1\,MHz$. A sinusoidal fit to the data (solid curve) yields visibility $V = 58 \pm 5\%$. **d**, Decay plot of the interference visibility. Blue points are single delay measurements on the maxima and minima of the curve, whereas green data points are extracted from fits, similar to **c**. The solid curve is a fit to an exponential decay. All error bars are 1 s.d.

dispersive coupling of the mode to defect states such as two-level fluctuators in the host material, which are a source of noise and dissipation in amorphous materials[43]. The surface of silicon is known to host a variety of states that have been found to affect the performance of quantum devices[44] and mechanical modes[32,45]. Optical driving of our particular device causes a saturation of the frequency jitter imposed on the mechanical mode. A more detailed study of the dynamics and prospects on an improved T_2^* will be the focus of future work. Similar two-level fluctuator noise is already known for a wide variety of systems, for which saturation driving of the states by different experimental means could offer a way to reduce the induced noise on the mode of interest[46,47].

The measured quantum decay T_1 and the coherence time T_2^* demonstrate the suitability of our high-Q mechanical system as a quantum memory operating in the low-loss telecommunication band. This was possible by employing a 2D phononic shield for mechanical isolation, small absorption heating in the optomechanical device compared to previous experiments and by devising a novel way to create and characterize mechanical superposition states. Combined with recent progress in coupling phonons to superconducting circuitry[33,48], this approach will also allow the realization of versatile hybrid architectures for quantum storage and transduction. We would like to note that, with improvements in the efficiencies, writing an arbitrary input state into the memory is in principle possible[49]. Future experiments will determine the nature and detailed properties of the frequency noise of the mechanical mode, which should lead the way to significant improvements of the coherence time of our devices.

Online content

Any methods, additional references, Nature Research reporting summaries, source data, extended data, supplementary information, acknowledgements, peer review information; details of author contributions and competing interests; and statements of data and code availability are available at https://doi.org/10.1038/s41567-020-0891-z.

Received: 21 August 2019; Accepted: 31 March 2020;
Published online: 18 May 2020

References

1. Kimble, H. J. The quantum internet. *Nature* **453**, 1023–1030 (2008).
2. Simon, C. Towards a global quantum network. *Nat. Photon.* **11**, 678–680 (2017).
3. Wang, Y. et al. Single-qubit quantum memory exceeding ten-minute coherence time. *Nat. Photon.* **11**, 646–650 (2017).
4. Crocker, C. et al. High purity single photons entangled with an atomic memory. *Opt. Express* **27**, 28143–28149 (2019).
5. Yang, S.-J., Wang, X.-J., Bao, X.-H. & Pan, J.-W. An efficient quantum light–matter interface with sub-second lifetime. *Nat. Photon.* **10**, 381–384 (2016).
6. Saunders, D. J. et al. Cavity-enhanced room-temperature broadband Raman memory. *Phys. Rev. Lett.* **116**, 090501 (2016).
7. Wang, Y. et al. Efficient quantum memory for single-photon polarization qubits. *Nat. Photon.* **13**, 346–351 (2019).
8. Kalb, N., Reiserer, A., Ritter, S. & Rempe, G. Heralded storage of a photonic quantum bit in a single atom. *Phys. Rev. Lett.* **114**, 220501 (2015).
9. Bradley, C. E. et al. A ten-qubit solid-state spin register with quantum memory up to one minute. *Phys. Rev. X* **9**, 031045 (2019).
10. Saglamyurek, E. et al. Quantum storage of entangled telecom-wavelength photons in an erbium-doped optical fibre. *Nat. Photon.* **9**, 83–87 (2015).
11. Dajczgewand, J., Gouët, J.-L., Louchet-Chauvet, A. & Chanelière, T. Large efficiency at telecom wavelength for optical quantum memories. *Opt. Lett.* **39**, 2711–2714 (2014).
12. Craiciu, I. et al. Nanophotonic quantum storage at telecommunication wavelength. *Phys. Rev. Appl.* **12**, 024062 (2019).
13. Askarani, M. F. et al. Storage and reemission of heralded telecommunication-wavelength photons using a crystal waveguide. *Phys. Rev. Appl.* **11**, 054056 (2019).

14. Manenti, R. et al. Circuit quantum acoustodynamics with surface acoustic waves. *Nat. Commun.* **8**, 975 (2017).
15. Bienfait, A. et al. Phonon-mediated quantum state transfer and remote qubit entanglement. *Science* **364**, 368–371 (2019).
16. Palomaki, T. A., Teufel, J. D., Simmonds, R. W. & Lehnert, K. W. Entangling mechanical motion with microwave fields. *Science* **342**, 710–713 (2013).
17. Ockeloen-Korppi, C. F. et al. Stabilized entanglement of massive mechanical oscillators. *Nature* **556**, 478–482 (2018).
18. Sletten, L. R., Moores, B. A., Viennot, J. J. & Lehnert, K. W. Resolving phonon Fock states in a multimode cavity with a double-slit qubit. *Phys. Rev. X* **9**, 021056 (2019).
19. Arrangoiz-Arriola, P. et al. Resolving the energy levels of a nanomechanical oscillator. *Nature* **571**, 537–540 (2019).
20. O'Connell, A. D. et al. Quantum ground state and single-phonon control of a mechanical resonator. *Nature* **464**, 697–703 (2010).
21. Chu, Y. et al. Creation and control of multi-phonon Fock states in a bulk acoustic-wave resonator. *Nature* **563**, 666–670 (2018).
22. Riedinger, R. et al. Non-classical correlations between single photons and phonons from a mechanical oscillator. *Nature* **530**, 313–316 (2016).
23. Purdy, T. P., Grutter, K. E., Srinivasan, K. & Taylor, J. M. Quantum correlations from a room-temperature optomechanical cavity. *Science* **356**, 1265–1268 (2018).
24. Chen, J., Rossi, M., Mason, D. & Schliesser, A. Entanglement of propagating optical modes via a mechanical interface. *Nat. Commun.* **11**, 943 (2020).
25. Hong, S. et al. Hanbury Brown and Twiss interferometry of single phonons from an optomechanical resonator. *Science* **358**, 203–206 (2017).
26. Anderson, M. D. et al. Two-color pump–probe measurement of photonic quantum correlations mediated by a single phonon. *Phys. Rev. Lett.* **120**, 233601 (2018).
27. Lee, K. C. et al. Entangling macroscopic diamonds at room temperature. *Science* **334**, 1253–1256 (2011).
28. Riedinger, R. et al. Remote quantum entanglement between two micromechanical oscillators. *Nature* **556**, 473–477 (2018).
29. Marinković, I. et al. An optomechanical Bell test. *Phys. Rev. Lett.* **121**, 220404 (2018).
30. Chan J. *Laser Cooling of an Optomechanical Crystal Resonator to its Quantum Ground State of Motion*. PhD thesis, California Institute of Technology (2012).
31. Kharel, P. et al. Ultra-high-*Q* phononic resonators on-chip at cryogenic temperatures. *APL Photon.* **3**, 066101 (2018).
32. MacCabe, G. S. et al. Phononic bandgap nano-acoustic cavity with ultralong phonon lifetime. Preprint at https://arxiv.org/abs/1901.04129 (2019).
33. Bochmann, J., Vainsencher, A., Awschalom, D. D. & Cleland, A. N. Nanomechanical coupling between microwave and optical photons. *Nat. Phys.* **9**, 712–716 (2013).
34. Forsch, M. et al. Microwave-to-optics conversion using a mechanical oscillator in its quantum groundstate. *Nat. Phys.* **16**, 69–74 (2020).
35. Duan, L. M., Lukin, M. D., Cirac, J. I. & Zoller, P. Long-distance quantum communication with atomic ensembles and linear optics. *Nature* **414**, 413–418 (2001).
36. Hofer, S. G., Wieczorek, W., Aspelmeyer, M. & Hammerer, K. Quantum entanglement and teleportation in pulsed cavity optomechanics. *Phys. Rev. A* **84**, 52327 (2011).
37. Galland, C., Sangouard, N., Piro, N., Gisin, N. & Kippenberg, T. J. Heralded single-phonon preparation, storage and readout in cavity optomechanics. *Phys. Rev. Lett.* **112**, 143602 (2014).
38. Safavi-Naeini, A. H. et al. Observation of quantum motion of a nanomechanical resonator. *Phys. Rev. Lett.* **108**, 033602 (2012).
39. de Riedmatten, H. et al. Direct measurement of decoherence for entanglement between a photon and stored atomic excitation. *Phys. Rev. Lett.* **97**, 113603 (2006).
40. Acín, A. et al. Device-independent security of quantum cryptography against collective attacks. *Phys. Rev. Lett.* **98**, 230501 (2007).
41. Lvovsky, A. I. & Mlynek, J. Quantum-optical catalysis: generating nonclassical states of light by means of linear optics. *Phys. Rev. Lett.* **88**, 250401 (2002).
42. Resch, K. J., Lundeen, J. S. & Steinberg, A. M. Quantum state preparation and conditional coherence. *Phys. Rev. Lett.* **88**, 113601 (2002).
43. Phillips, W. A. Two-level states in glasses. *Rep. Prog. Phys.* **50**, 1657 (1987).
44. Müller, C., Cole, J. H. & Lisenfeld, J. Towards understanding two-level-systems in amorphous solids: insights from quantum circuits. *Rep. Prog. Phys.* **82**, 124501 (2019).
45. Meenehan, S. M. et al. Silicon optomechanical crystal resonator at millikelvin temperatures. *Phys. Rev. A* **90**, 011803 (2014).
46. Constantin, M., Yu, C. C. & Martinis, J. M. Saturation of two-level systems and charge noise in Josephson junction qubits. *Phys. Rev. B* **79**, 094520 (2009).
47. Behunin, R. O., Kharel, P., Renninger, W. H. & Rakich, P. T. Engineering dissipation with phononic spectral hole burning. *Nat. Mater.* **16**, 315–321 (2017).
48. Kalaee, M. et al. Quantum electromechanics of a hypersonic crystal. *Nat. Nanotechnol.* **14**, 334–339 (2019).
49. Choi, K. S., Deng, H., Laurat, J. & Kimble, H. J. Mapping photonic entanglement into and out of a quantum memory. *Nature* **452**, 67–71 (2008).

Data availability

Source data are available for this paper. All other data that support the plots within this paper and other findings of this study are available from the corresponding author upon reasonable request.

Code availability

The QuTiP code used for the simulations in the Supplementary Information is available on GitHub (https://github.com/GroeblacherLab/quantum_memory_code).

Acknowledgements

We thank M. Forsch, B. Li, M. Vlassov and I. Yang for experimental support and D. Bothner for valuable discussions. We also acknowledge assistance from Kavli Nanolab Delft. This work is supported by the Foundation for Fundamental Research on Matter (FOM) Projectruimte grants (15PR3210, 16PR1054), the European Research Council (ERC StG Strong-Q, 676842) and by the Netherlands Organization for Scientific Research (NWO/OCW), as part of the Frontiers of Nanoscience program, as well as through a Vidi grant (680-47-541/994). B.H. and R.S. acknowledge funding from the European Union under a Marie Skłodowska-Curie COFUND fellowship.

Author contributions

A.W., I.M. and S.G. planned the experiment and performed the device design. I.M. fabricated the sample and A.W. performed the measurements. A.W., B.H., R.S. and S.G. analysed the data and wrote the manuscript with input from all authors. S.G. supervised the project.

Competing interests

The authors declare no competing interests.

Additional information

Supplementary information is available for this paper at https://doi.org/10.1038/s41567-020-0891-z.

Correspondence and requests for materials should be addressed to S.G.